Journal of Advanced Ceramics
2022, **11**(8): 1319–1329
https://doi.org/10.1007/s40145-022-0614-2
ISSN 2226-4108
CN 10-1154/TQ

Research Article

Delayed stress memory by $CaAl_2O_4:Eu^{2+}$ mechanoluminescent phosphor with defect engineering regulation

Yiyu CAI[a,b,†], Sibo LIU[c,†], Lei ZHAO[d], Chao WANG[b], Hongyu LV[b], Bitao LIU[e], Jianbei QIU[b], Xuhui XU[a,b,*], Xue YU[a,b,*]

[a]*School of Mechanical Engineering, Institute for Advanced Materials, Chengdu University, Chengdu 610106, China*
[b]*College of Materials Science and Engineering, Key Laboratory of Advanced Materials of Yunnan Province, Kunming University of Science and Technology, Kunming 650093, China*
[c]*Department of Orthopedics, The First People's Hospital of Yunnan Province, Kunming 650093, China*
[d]*School of Physics and Opto-Electronic Technology, Baoji University of Arts and Sciences, Baoji 721016, China*
[e]*Research Institute for New Materials Technology, Chongqing University of Arts and Sciences, Chongqing 402160, China*

Received: February 3, 2022; Revised: May 4, 2022; Accepted: May 17, 2022

Abstract: Real-time stress sensing based on mechanoluminescence materials has been widely studied for structural health monitoring of bridges, buildings, high-pressure vessels, and other infrastructure surfaces. However, this approach is difficult to detect the stress information of closed mechanical structures. Here, we propose a delayed stress memory strategy to record the stress information of closed mechanical structure by the flexible film composed with $CaAl_2O_4:Eu^{2+},Sm^{3+}$ phosphor. After the force is applied, the optical information on the film can be read out by the near-infrared laser after a period of time without real-time monitoring, and the stress distribution information of bearings and gears in the engine can be obtained. Furthermore, the regulation of trap depth from 0.662 to 1.042 eV allows the captured carriers to remain in the traps for a long time without being released as long persistent luminescence, which is beneficial to the delayed stress memory. Therefore, this work promotes the application prospect of mechanoluminescence materials in stress sensing, and provides a new idea to record the stress information of closed mechanical structures.

Keywords: delayed stress memory; mechanoluminescent film; stress information; defect engineering; closed mechanical structure

1 Introduction

Mechanoluminescence (ML) is the phenomenon that solid materials emit visible or invisible light under mechanical stimuli such as compression, fracture, impact, grinding, and stretching [1–4]. In recent years, ML has been widely studied due to its promising applications in stress sensing [5], E-signature systems [6], artificial skins [7], structure damage diagnosis platforms [8], information storage [9], anti-counterfeiting [10], and biomedical engineering [11]. Depending on the specific nature of the mechanical stimulation and whether it

† Yiyu Cai and Sibo Liu contributed equally to this work.

* Corresponding authors.
E-mail: X. Xu, xuxuh07@126.com;
X. Yu, yuyu6593@126.com

destroys ML material, ML can be divided into two categories: destructive ML including fractoluminescence (FML) and non-destructive ML including elasticoluminescence (EML) and triboluminescence (TML) [3,12]. Compared with FML and TML, EML has drawn extensive attention in stress detection and visualizing stress distribution due to the advantages of recoverable emission and the linear relation between ML intensity and the magnitude of the loading force. In particular, Xu *et al*. firstly reported the EML from ZnS:Mn [13] and $SrAl_2O_4:Eu^{2+}$ [14], and examined the structural damage of the bridge by attaching several ML films embedded with $SrAl_2O_4:Eu^{2+}$ particles to the cracks being visible on a concrete girder of the bridge [8]. Klein *et al*. [15,16] also proposed to determine the stress field by coating the aircraft surface with ML sensor materials, and the sensor materials generate a sensitive spectral response to the applied pressure in a wind tunnel. Subsequently, a large number of EML materials have also been developed as depicted in Table 1, which exhibits distinctive ML performance of intense brightness, high mechanical sensitivity, abundant emission wavelength, and other properties. Although stress sensing based on these ML materials has realized remote, real-time, and large-area monitoring of stress information for macroscopic infrastructure surfaces, it is still difficult to detect the stress information of closed mechanical structures, and it should be noticed that the ML properties are always accompanied with a long persistent luminescence (LPL) behavior.

Typically, the excited carriers are partially captured by the trap centers in the ML material once exposed to ultraviolet or visible light. These captured carriers are released under appropriate mechanical stimuli and eventually participate in the light emission process, producing the ML [3,10]. Nevertheless, the carriers captured by the trap centers would be thermally unstable if the trap distribution in the matrix is relative shallower, and then the de-trapping process occurs under thermal disturbance at room temperature, eventually resulting in LPL [53], which is fundamentally detrimental to the ML output. Herein, Rahimi *et al*. [54] presented an approach of increasing the delay time to reduce the LPL intensity and improve the signal-to-noise ratio (SNR) of ML accordingly. The ML material firstly was exposed to the excitation light source and then deposited in the dark for some time before applying the mechanical stimulation, which endows the response to the stress information more effectively. Recently, Zhang *et al*. [33,55] also proposed a strategy of sacrificing the trap density to achieve high SNR of ML materials for stress imaging. Although these results provide a possibility for obtaining high contrast ML performance, the ML behavior is inevitable to be impacted by increasing the delay time or sacrificing trap density. Therefore, it is of great importance for the ML materials to achieve

Table 1 Representative available EML materials

Composition	λ_{LPL} (nm)	λ_{ML} (nm), color	Trap depth (eV)	Ref.
$SrAl_2O_4:Eu^{2+}$	510	510, green	0.606, 0.71, 0.84	[14,17–19]
$Ca_2Al_2SiO_7:Ce^{3+}$	402	402, blue	0.866–1.286	[20–22]
$Sr_2MgSi_2O_7:Eu^{2+}$	464	464, blue	0.75	[23–25]
$CaYAl_3O_7:Ce^{3+}$	421	421, blue	0.706	[21,26]
$SrMg_2(PO)_4:Eu^{2+}$	412	412, blue	0.65, 0.78	[27,28]
$LiNbO_3:Pr^{3+}$	619	619, red	0.65	[29–31]
$Ca_2Nb_2O_7:Pr^{3+}$	613	613, red	0.52, 0.63	[32,33]
$(Ba,Ca)TiO_3:Pr^{3+}$	613	613, red	0.65	[34,35]
$Ca_3Ti_2O_7:Pr^{3+}$	615	615, red	0.65	[36]
$BaSi_2O_2N_2:Eu^{2+}$	493	493, bluish green	0.706	[37,38]
$CaZr(PO_4)_2:Eu^{2+}$	474	474, cyan	0.65, 0.82, 1.01	[39]
$Sr_3Sn_2O_7:Sm^{3+}$	570, 582, 610, 624	570, 582, 610, 624, reddish orange	0.882, 0.960	[40–42]
$ZnGa_2O_4:Mn^{2+}$	505	505, green	0.71	[43,44]
$MgGa_2O_4:Mn^{2+}$	506	506, green	0.654	[43,45]
$ZnS:Mn^{2+}$	585	585, yellow	0.68, 0.72	[7,46,47]
$CaZnOS:Mn^{2+}$	610	610, red	0.7	[48–50]
$BaZnOS:Mn^{2+}$	584, 610	584, 610, orange, red	0.898	[51,52]

intense stress information free from the LPL interference, thereby improving the SNR to satisfy the requirements of advanced practical applications.

In this work, we regulate the trap depth from 0.662 to 1.042 eV by introducing foreign Ln^{3+} ions in $CaAl_2O_4:Eu^{2+}$ (CAO:Eu^{2+}), which allows the carriers in the regulated deep traps to remain for a long time and hardly be affected by the thermal disturbance at room temperature. Furthermore, it is also found that, the carriers captured by the deep traps not only can be released by the mechanical stimulation for achieving ML but also be induced by infrared (980 nm) irradiation to produce the photo-stimulated luminescence (PSL). Therefore, we propose a delayed stress memory strategy to record the stress information of closed mechanical structures. The results indicate that the stress distribution information of bearings and gears in the engine can be obtained by recording the PSL intensity difference of the flexible films at the positions with and without the mechanical stimulation after applying force. This non-real-time stress sensing opens a new path for detecting and recording the stress information of closed mechanical structures.

2 Experimental

2. 1 Synthesis of ML phosphors

CAO:0.0025Eu^{2+}, CAO:0.0025Eu^{2+},$y$$Dy^{3+}$ (y = 0.0005, 0.001, 0.00125, 0.0025, and 0.0075), CAO:0.0025Eu^{2+}, 0.01Y^{3+}, CAO:0.0025Eu^{2+},0.01Tm^{3+}, CAO:0.0025Eu^{2+}, 0.01Nd^{3+}, and CAO:0.0025Eu^{2+},0.01Sm^{3+} phosphors were synthesized by using a high-temperature solid-state reaction method. Stoichiometric starting materials Ca_2CO_3 (99.99%), Al_2O_3 (99.99%), Eu_2O_3 (99.99%), Dy_2O_3 (99.99%), Y_2O_3 (99.99%), Tm_2O_3 (99.99%), Nd_2O_3 (99.99%), and Sm_2O_3 (99.99%) with few H_3BO_3 (99.99%) as sintering flux were homogeneously mixed in an agate mortar and subsequently transferred into an alumina crucible. The mixtures were sintered at 1380 ℃ for 4 h in a horizontal tube furnace under reduced atmosphere (5%H_2 + 95%N_2). After cooling to room temperature, the ML phosphors were ground for further use.

2. 2 Fabrication of ML composite films

To quantitatively analyze the ML properties, the synthesized phosphors were ground and sieved (300 mesh/in). The phosphors were mixed with polydimethylsiloxane (PDMS, Sylgard 184, Dow Corning) in a weight ratio of 2 : 1. The mixture was poured into a rectangle mold (45 mm × 25 mm × 1 mm) and then put in a vacuum drying oven at 60 ℃ for 4 h. After the curing process, an ML film with an average thickness of 1–2 mm was obtained.

2. 3 Characterizations

A D8 ADVANCE/Germany Bruker X-ray diffractometer (XRD) with Cu Kα radiation (λ = 1.5405 Å) operating at 40 kV and 30 mA was employed to characterize the crystalline phases of the obtained powders, and the raw XRD data were further analyzed by the Rietveld refinement method (GSAS software package). The surface morphology and elemental mapping were characterized by a field-emission SEM instrument (SU8010, Hitachi) with an energy dispersive X-ray (EDX) spectroscope system. Photoluminescence (PL) and photoluminescence excitation (PLE) spectra were recorded by a Hitachi F7000 fluorescence spectrophotometer with an excitation source of 150 W Xe lamp. The thermoluminescence (TL) curves were measured with an FJ-427A TL meter (Beijing Nuclear Instrument Factory). The weight of the measured powders was constant (0.002 g). Before the TL measurement, the samples were firstly exposed to the radiation from sunlight for about 15 min, and then heated from room temperature to 550 K at a rate of 60 K/min. The ML intensity of the films was investigated with a lab-built system that comprises a universal testing machine (AG-X, Shimadzu) (Fig. S1 in the Electronic Supplementary Material (ESM)) and a photo-counting system, which consisted of a photomultiplier tube (55777, Oriel Instruments) and a photo-counter (C9692, Hamamatsu). A fiber spectrometer with a wavelength range from 200 to 1000 nm (QE Pro, Ocean Optics) was applied to record the PSL and ML spectra. All optical photos were taken by a digital camera (D7100, Nikon).

3 Results and discussion

Figure 1(a) depicts the XRD patterns of the CAO:Eu^{2+}, Ln^{3+} (Ln = Dy, Tm, Nd, Y, and Sm) phosphors, which match well with the standard profile (JCPDS No. 70-0134). It indicates that all samples are in a pure phase, and the introduction of Eu^{2+} and Ln^{3+} ions hardly produces a significant impurity phase. Figures 1(b) and

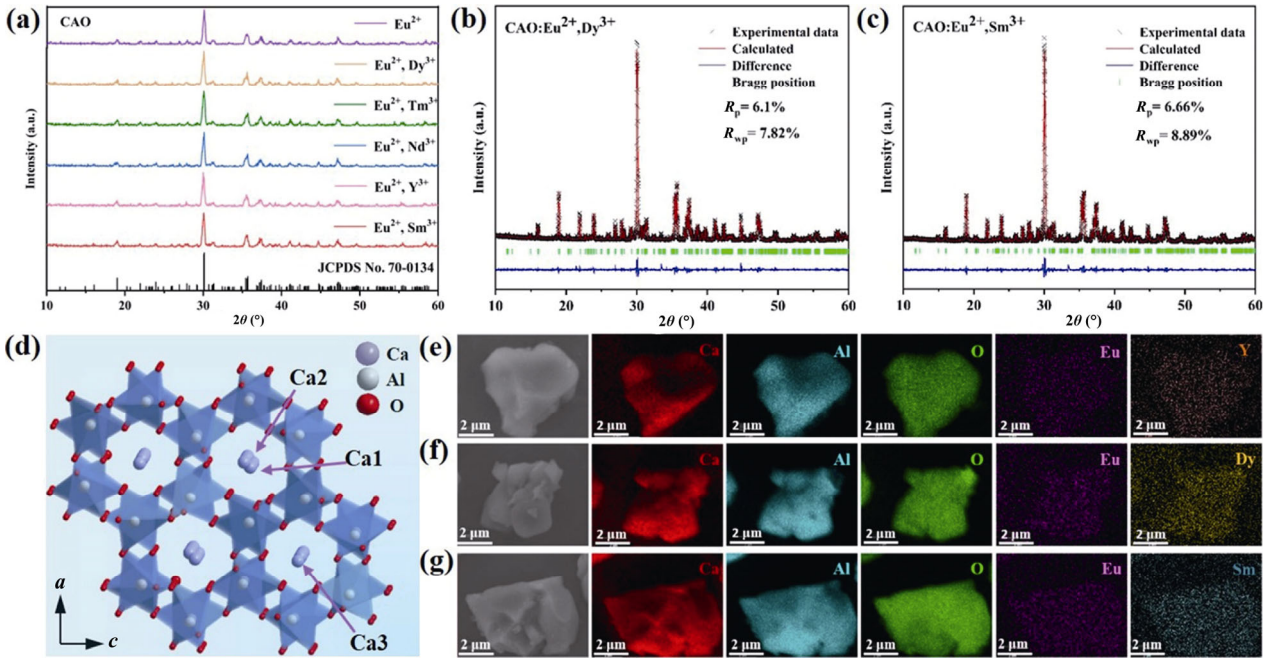

Fig. 1 (a) XRD patterns of CAO:Eu^{2+},Ln^{3+} (Ln = Dy, Tm, Nd, Y, and Sm). Rietveld refinement of XRD profiles: (b) CAO:Eu^{2+},Dy^{3+}, and (c) CAO:Eu^{2+},Sm^{3+}. (d) Crystal structure of CAO. SEM images and elemental mappings of (e) CAO:Eu^{2+},Y^{3+}, (f) CAO:Eu^{2+},Dy^{3+}, and (g) CAO:Eu^{2+},Sm^{3+}.

1(c) display the Rietveld refinement of XRD patterns of CAO:Eu^{2+},Dy^{3+} and CAO:Eu^{2+},Sm^{3+}, respectively. The refinement parameter values are calculated to be R_p = 6.1%, R_{wp} = 7.82% of CAO:Eu^{2+},Dy^{3+}, and R_p = 6.66%, R_{wp} = 8.89% of CAO:Eu^{2+},Sm^{3+}, which further confirms the pure phase of the as-obtained samples. According to the crystallographic data, CAO belongs to the monoclinic system with a space group of P21/n (14), and there are three different sites of Ca^{2+} ions. Two sites of Ca1 and Ca2 are coordinated with six oxygen ions having different bond lengths, whereas the third site of Ca3 is coordinated with nine oxygen ions [55–57]. All calcium ions array in a line along the *b*-axis, and Ca3 ions align more regularly compared with Ca1 and Ca2 (Fig. 1(d)). Considering the ionic radii and valence, the Ca3 (r = 1.00 Å, coordination number (CN) = 6, and r = 1.18 Å, CN = 9) sites are preferentially replaced by Eu^{2+} (r = 1.17 Å), Dy^{3+} (r = 0.91 Å), Tm^{3+} (r = 0.88 Å), Nd^{3+} (r = 0.98 Å), Y^{3+} (r = 0.88 Å), and Sm^{3+} (r = 0.95 Å) ions [58]. The crystal morphology and X-ray energy dispersive spectrum (EDS) analysis with elemental mappings (Figs. 1(e)–1(g) and Fig. S2 in the ESM) illustrates that all elements are homogeneously distributed within the corresponding particle, and further confirms the successful incorporation of Eu^{2+} and Ln^{3+} ions.

As illustrated in Fig. 2(a), the as-prepared CAO:Eu^{2+} phosphor is further composited with the transparent PDMS matrix to form a CAO:Eu^{2+}/PDMS composite film with a rectangle shape. Since the CAO:Eu^{2+}-based materials are the typical long-persistent luminescence systems, the CAO:Eu^{2+}/PDMS composite film firstly is exposed to the excitation light source, and then deposited in the dark for some time to eliminate the interference of LPL before applying the mechanical stimulation. When mechanical stimuli such as stretching, rubbing, and folding are applied, intense blue light emission of CAO:Eu^{2+}/PDMS film is observed with naked eyes, which proves the ML behavior originated from the corresponding film (Fig. 2(b)). Figure 2(c) presents the PL, LPL, and ML spectra of CAO:Eu^{2+}/PDMS film. The ML spectrum is similar to the PL and LPL spectra, showing a broadband ranging from 410 to 500 nm with a maximum emission peak located at 440 nm ascribed to the transition from $4f^6 5d$ to $4f^7$ level of Eu^{2+} ions [59–61]. Figure 2(d) shows the ML response of CAO:Eu^{2+}/PDMS film under the stretching force, and the peak intensity of ML has a significant decay under the consecutive stretching–releasing cycles, which is attributed to the gradual release of carriers in the trap centers. Moreover, the ML and TL intensities of film for sunlight filling and thermal bleaching after 5 cycles are recorded, as shown in Fig. 2(e). The results show that there is obvious ML after the trap centers are filled

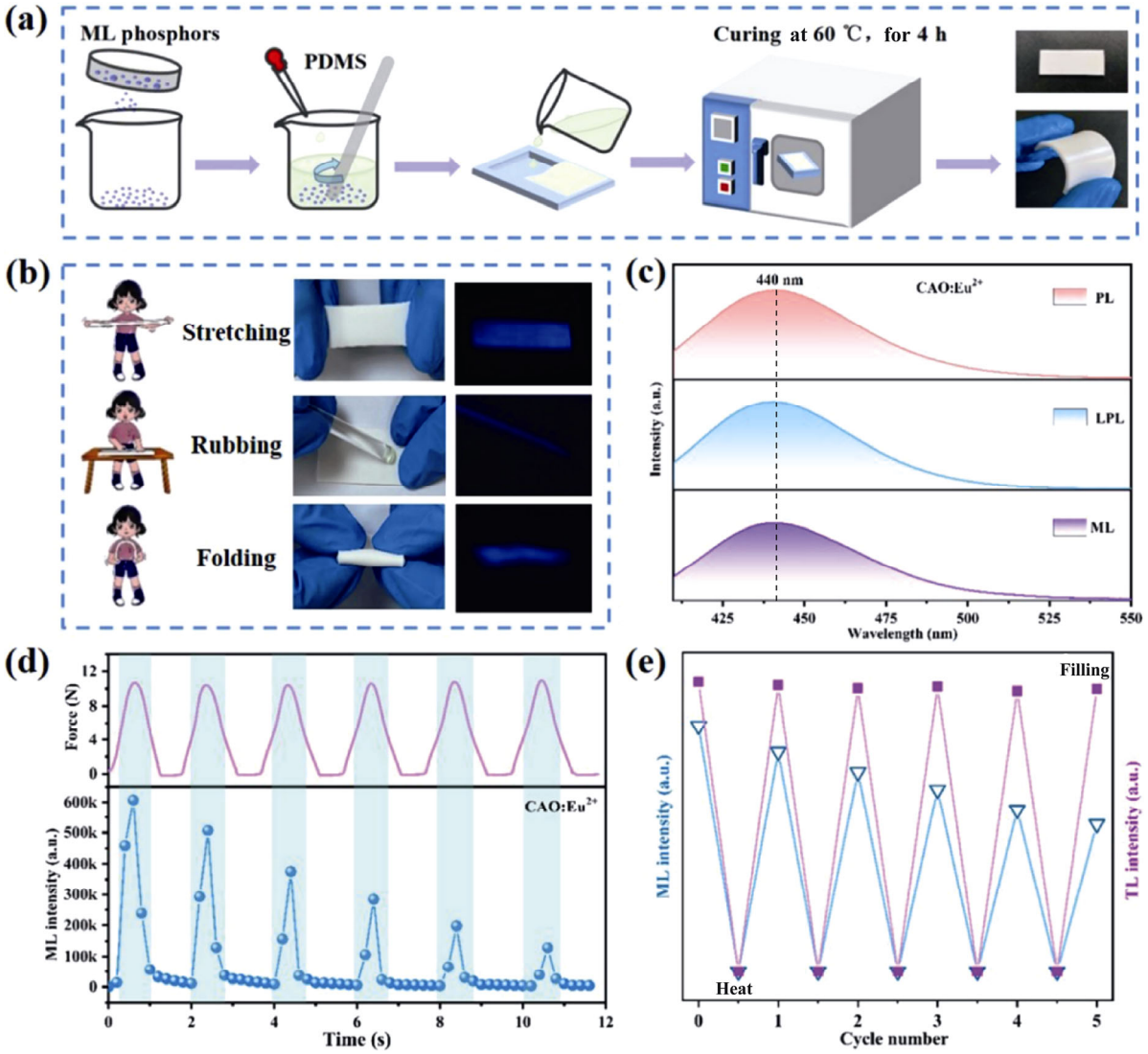

Fig. 2 (a) Schematic of the fabrication process of the corresponding CAO:Eu^{2+}/PDMS film. (b) ML photographs of the as-fabricated film under the mechanical stimuli of stretching, rubbing, and folding. (c) PL, LPL, and ML spectra of CAO:Eu^{2+}/PDMS film. (d) ML decay behavior of CAO:Eu^{2+}/PDMS film under the consecutive stretching–releasing for 6 cycles. (e) Cyclic stability test of sunlight filling and thermal bleaching of the induced ML and TL change of CAO:Eu^{2+}/PDMS film.

with carriers, while the ML disappears after the carriers in the trap centers are thermally released (at 200 ℃ for 30 min), which further proves that the ML behavior is derived from the release of carriers in the trap centers under the mechanical stimulation. Furthermore, the intensity of ML gradually decreases with the increase of the number of cycles, for the PDMS matrix is inclined to be damaged during the process of thermal treatment and hardly to completely recovered.

Generally, the concentration and distribution of trap centers have been identified as critical factors affecting the ML performance [62,63]. Hence, the ML performance of CAO:0.0025Eu^{2+},$y$$Dy^{3+}$/PDMS film ($y$ = 0.0005, 0.001, 0.00125, 0.0025, and 0.0075) is evaluated to study the effect of trap concentration on the ML properties. Figure 3(a) gives the ML spectra of CAO:0.0025Eu^{2+},$y$$Dy^{3+}$/PDMS film, which has similar broadbands, indicating the same emitting center for those films and the introduced Dy^{3+} ions act as the trap centers. Figure 3(b) shows the change of the ML intensity with the increasing dopants, which reaches the maximum at y = 0.0025 and then decreases. In addition, as shown in Fig. 3(c), the TL curves of CAO:0.0025Eu^{2+},$y$$Dy^{3+}$/PDMS film are recorded, and the TL intensity also reaches the maximum value at y = 0.0025, which is consistent with the behavior of ML in Figs. 3(a) and 3(b). The results indicate that the intensity of ML is positively correlated with the

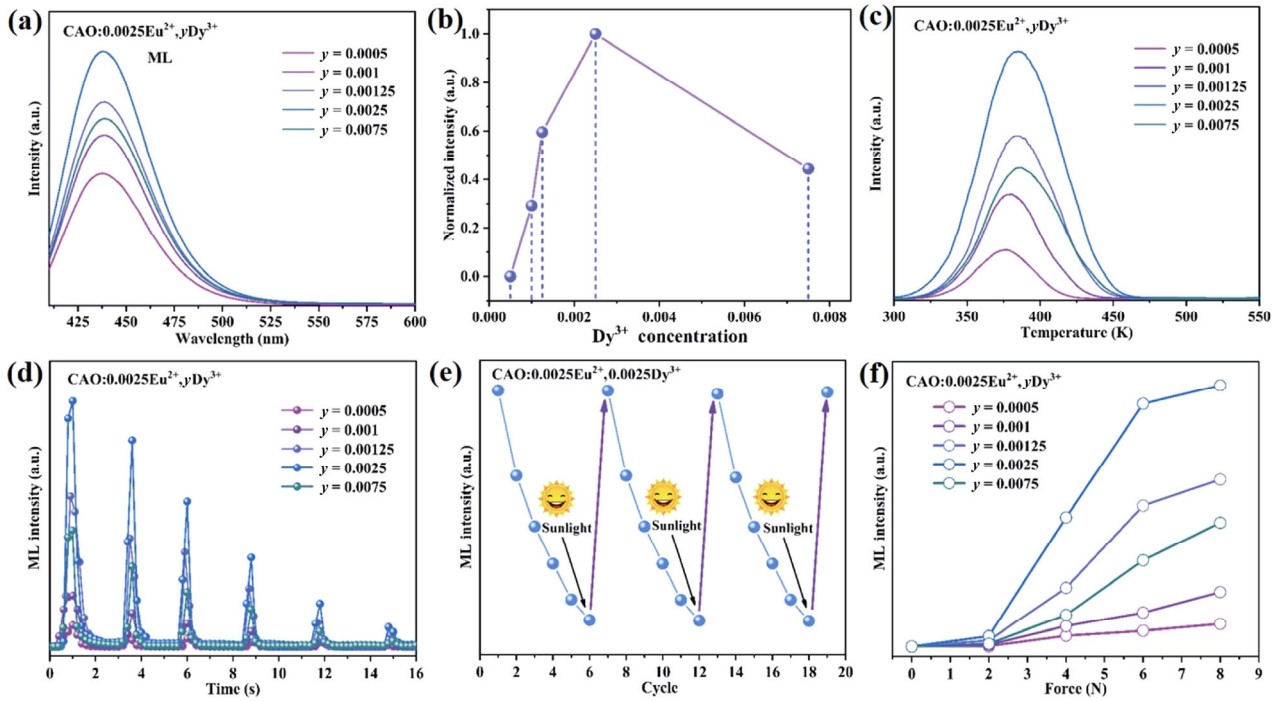

Fig. 3 (a) ML spectra, (b) dependence of ML intensity on the doping concentration, (c) TL curves, and (d) ML decay behavior of CAO:0.0025Eu^{2+},*y*Dy^{3+}/PDMS film. (e) ML recovery behavior of CAO:0.0025Eu^{2+},0.0025Dy^{3+}/PDMS film. (f) Dependence of ML intensity on the stretching forces of CAO:0.0025Eu^{2+},*y*Dy^{3+}/PDMS film.

concentration of trap centers. Figure 3(d) displays the ML response of CAO:0.0025Eu^{2+},*y*Dy^{3+}/PDMS film under the consecutive stretching–releasing cycles, and the intensity of ML exhibits a significant decay with the increase of the number of cycles, which is caused by the gradual release of carriers in the trap centers under the mechanical stimulation. However, it is noted that, the ML intensity can be fundamentally recovered after the sunlight irradiation, as shown in Fig. 3(e), indicating the excellent reproducibility of ML in CAO:0.0025Eu^{2+},0.0025Dy^{3+}/PDMS film. Figure 3(f) plots the dependence of ML intensity on the stretching forces of CAO:0.0025Eu^{2+},*y*Dy^{3+}/PDMS film, which demonstrates that the ML intensity increases monotonously with the increase of the stretching force. Moreover, the typical ML images of CAO:0.0025Eu^{2+}, *y*Dy^{3+}/PDMS film under different stretching forces are shown in Fig. S4 in the ESM.

To further verify the reliability of the above conclusions, the trap concentration is also adjusted by introducing different Ln^{3+} ions (i.e., Dy^{3+}, Tm^{3+}, and Nd^{3+}) into CAO:Eu^{2+}. The TL curves of CAO:Eu^{2+},Dy^{3+}/PDMS, $CaAl_2O_4$:Eu^{2+},Tm^{3+}/PDMS, and $CaAl_2O_4$:Eu^{2+}, Nd^{3+}/PDMS film are displayed in Fig. S5(a) in the ESM. The trap depth does not change in a certain range, while the trap concentration changes greatly, wherein the trap concentration of CAO:Eu^{2+},Dy^{3+}/PDMS film is the highest. Figure S5(b) in the ESM gives the ML responses of CAO:Eu^{2+},Dy^{3+}/PDMS, CAO:Eu^{2+},Tm^{3+}/PDMS, and CAO:Eu^{2+},Nd^{3+}/PDMS films under the consecutive stretching–releasing cycles. The results show that CAO:Eu^{2+},Dy^{3+}/PDMS film presents the maximum ML intensity under the same stretching force. This phenomenon can also be clearly observed in the ML images under different stretching forces (Fig. S5(c) in the ESM). Therefore, the ML intensity is confirmed to be linearly correlated with the trap concentration.

The effect of the distribution of trap on the ML properties is further clarified. Figure S6 in the ESM shows the normalized TL curves of Ln^{3+} (Ln = Dy, Tm, Nd, Y, and Sm) co-doped in CAO:Eu^{2+}. The trap depth corresponding to the TL peak is estimated with the following approximate in Eq. (1) [64]:

$$E_T = T_m / 500 \quad (1)$$

where E_T is the calculated trap depth, and T_m is the maximum peak temperature of the TL curve (in Kelvin, K). Therefore, the adjustment of trap depth from 0.662 to 1.042 eV is achieved for the foreign introduced Ln^{3+} ions. Figure S7 in the ESM displays the LPL images of the CAO:Eu^{2+},Y^{3+}/PDMS, CAO:Eu^{2+},Dy^{3+}/PDMS, and

CAO:Eu^{2+},Sm^{3+}/PDMS film. The CAO:Eu^{2+},Y^{3+}/PDMS and CAO:Eu^{2+},Dy^{3+}/PDMS films exhibit longer LPL duration time compared with CAO:Eu^{2+},Sm^{3+}/PDMS film. Therefore, we speculate that the CAO:Eu^{2+},Sm^{3+}/PDMS film may have higher SNR in ML performance. Figures 4(a)–4(c) provide the ML decay behavior of CAO:Eu^{2+},Y^{3+}/PDMS, CAO:Eu^{2+},Dy^{3+}/PDMS, and CAO:Eu^{2+},Sm^{3+}/PDMS films under the consecutive stretching–releasing for 6 cycles. The ML of CAO:Eu^{2+},Y^{3+}/PDMS and CAO:Eu^{2+},Dy^{3+}/PDMS films have strong LPL background, but the ML of CAO:Eu^{2+},Sm^{3+}/PDMS film is free from LPL background, which ascribes to the fact that the carriers in the deep traps are more difficult to be released under thermal disturbance, compared with shallow traps. Furthermore, the CAO:Eu^{2+},Sm^{3+}/PDMS film shows higher SNR ($>$ 60-fold in the CAO:Eu^{2+},Y^{3+} and $>$ 40-fold CAO:Eu^{2+},Dy^{3+}) (Fig. 4(d)), which is beneficial for the accurate stress information detection of the closed mechanical structures. The results show that the high SNR of ML performance is achieved by the defect engineering regulation.

Therefore, we proposed and illustrated the mechanism for the ML as shown in Fig. 4(e). Firstly, under the irradiation of sunlight, the electrons are excited from the valence band (VB) to the conduction band (CB), and then these electrons are partially captured by the trap levels. When the mechanical stimulation is applied, the trapped electrons can be released and come back to the $4f^65d$ level of Eu^{2+}. Finally, the electrons return to the ground state and emit blue emission (ML). However, when the trap depth is shallower (i.e., CAO:Eu^{2+},Y^{3+} and CAO:Eu^{2+},Dy^{3+}), thermally-induced de-trapping can also occur at room temperature, resulting in the

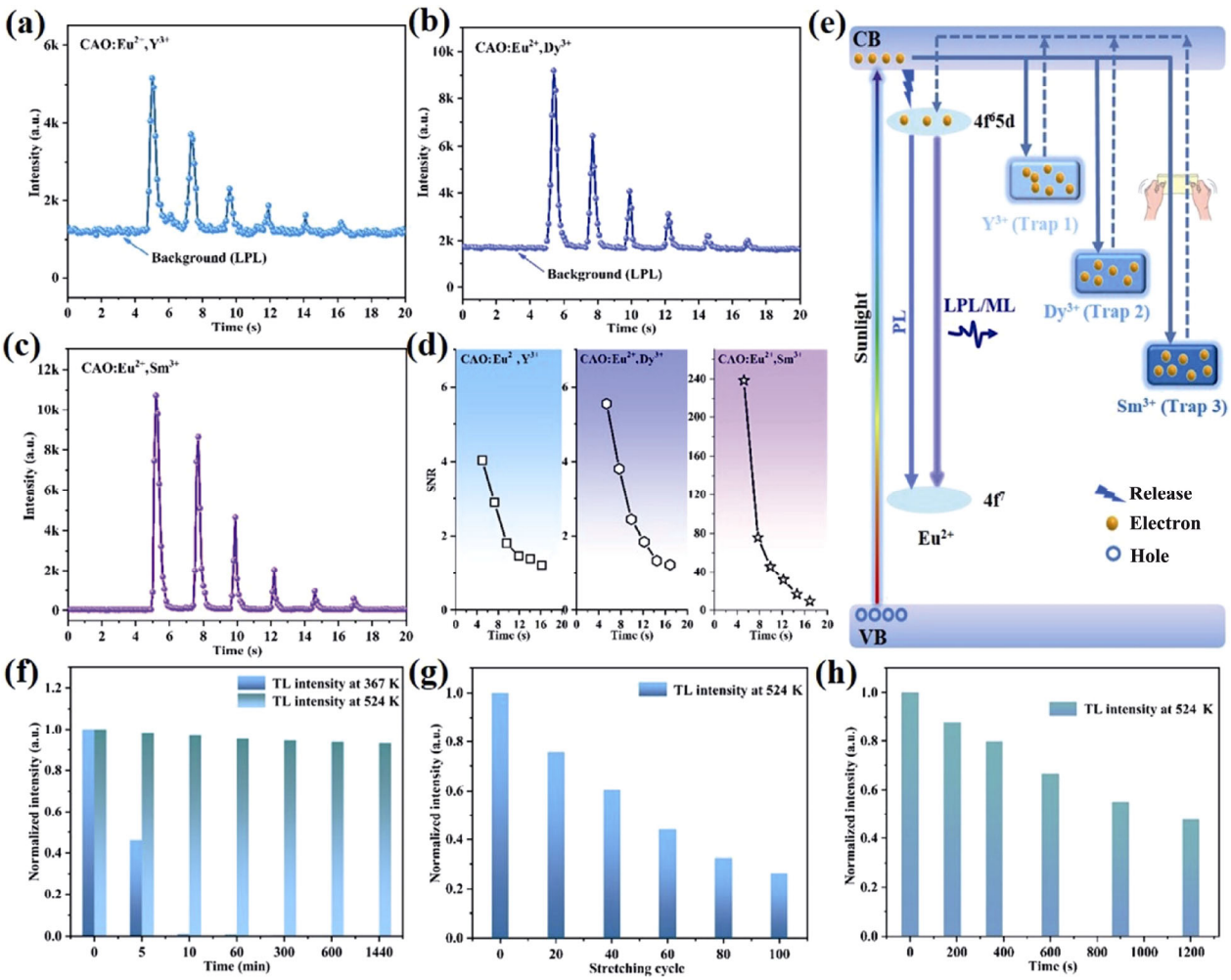

Fig. 4 ML decay behavior of (a) CAO:Eu^{2+},Y^{3+}/PDMS, (b) CAO:Eu^{2+},Dy^{3+}/PDMS, and (c) CAO:Eu^{2+},Sm^{3+}/PDMS films under the consecutive stretching–releasing for 6 cycles, and (d) the corresponding SNR results. (e) Proposed schematic mechanism for the ML behavior. TL intensities of CAO:Eu^{2+},Sm^{3+}/PDMS film at 367 and 524 K varied with the (f) deposit time at room temperature, (g) stretching cycles, and (h) irradiation time under 980 nm irradiation, respectively.

ML accompanied by LPL behavior, which is why CAO:Eu^{2+},Y^{3+} and CAO:Eu^{2+},Dy^{3+} show lower SNR.

The release process of carriers in the trap centers of CAO:Eu^{2+},Sm^{3+}/PDMS film is further investigated. The TL curves and the corresponding intensity of trap centers at 367 and 524 K varied with the deposited time at room temperature in the dark for CAO:Eu^{2+},Sm^{3+}/PDMS film as depicted in Figs. 4(f) and S8(a) in the ESM. The results indicate the TL intensity at 367 K decreases gradually with the prolonged time, while the TL intensity of trap centers at 524 K is constant (after 1440 min), indicating that carriers in deep trap centers can be stored for a long time at room temperature. When the mechanical stimuli are applied on the CAO:Eu^{2+},Sm^{3+}/PDMS film, the TL intensity of trap centers at 524 K decreases gradually with the increase of stretching cycle (Figs. 4(g) and S8(b) in the ESM), which manifests that the carriers in the deep trap centers can be released and produce ML under the mechanical stimulation. Moreover, as shown in Figs. 4(h) and S8(c) in the ESM, the TL intensity of the trap centers at 524 K decreases gradually with the 980 nm irradiation time prolonging, indicating that the carriers in the deep trap centers can also be released in the form of PSL under 980 nm irradiation.

Based on the above results, a delayed stress memory method is proposed to record the stress distribution information for the closed mechanical structures by CAO:Eu^{2+},Sm^{3+}/PDMS film. (i) and (ii) in Fig. 5(a) show photographs of the engine and the bearing of its internal parts, respectively. Firstly, the prepared flexible CAO:Eu^{2+},Sm^{3+}/PDMS film is exposed to sunlight radiation for about 15 min, and then deposited inside the engine bearing and applied mechanical stimulation ((iii) in Fig. 5(a)). Figure 5(b) gives the cross-sectional SEM images of the as-fabricated CAO:Eu^{2+},Sm^{3+}/PDMS film. The film possesses a thickness of 1 mm with the CAO:Eu^{2+},Sm^{3+} particles being evenly distributed, which ensures the uniformity of their optical properties. Under the mechanical stimulation, some of the carriers stored in the trap centers can be released in the form of ML, and the remaining carriers can then be read out by the irradiation of a 980 nm laser. The PSL image and corresponding intensity map are shown in Fig. 5(c),

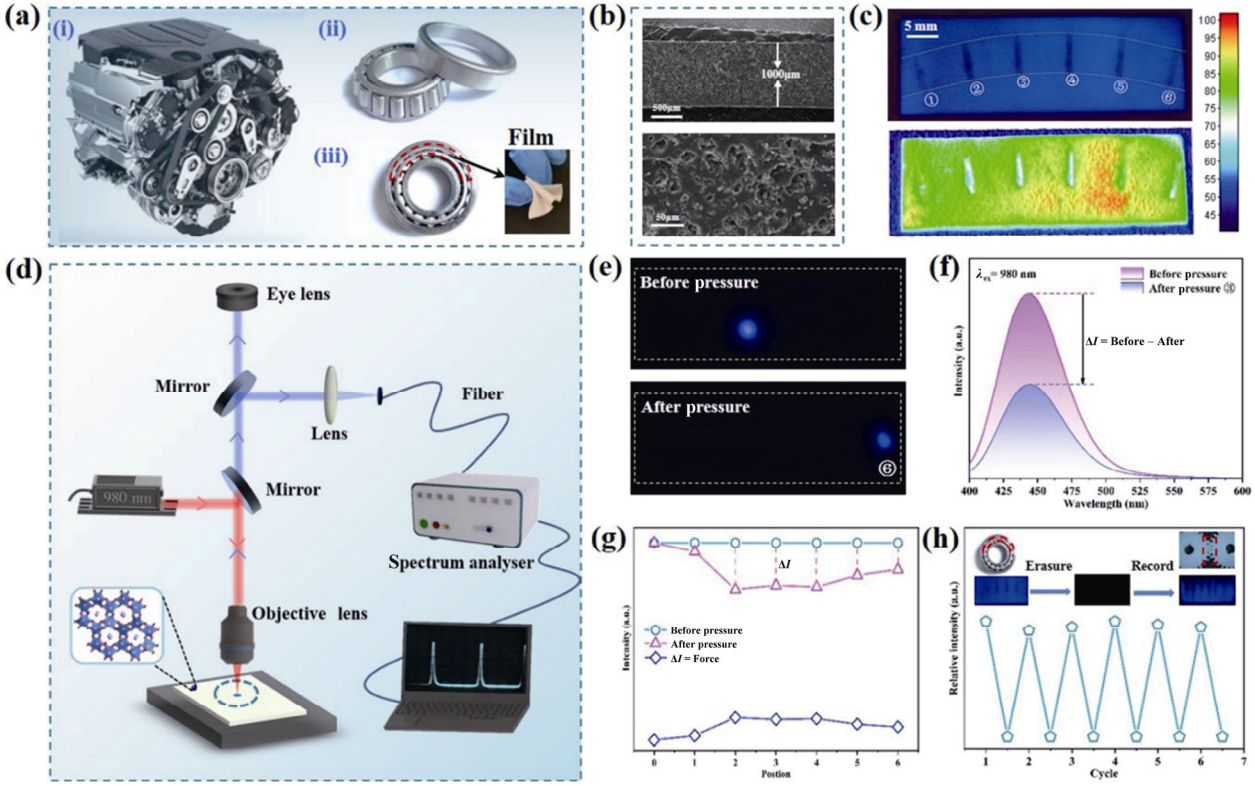

Fig. 5 (a) Photographs of (i) the engine, (ii) the engine bearing, and (iii) the CAO:Eu^{2+},Sm^{3+}/PDMS film attached to the inside of an engine bearing. (b) Cross-sectional SEM images, and (c) PSL image and PSL intensity map of the as-fabricated CAO:Eu^{2+},Sm^{3+}/PDMS film. (d) Experimental setup for the PSL measurement, and (e) PSL images and (f) PSL emission spectra of the CAO:Eu^{2+},Sm^{3+}/PDMS film before and after the mechanical stimuli. (g) PSL intensity and corresponding difference of the CAO:Eu^{2+},Sm^{3+}/PDMS film. (h) Erasable and rewritable cycles of stress information.

and the stripe between light and dark can be clearly seen, which indirectly shows the stress information inside the engine bearing.

Figure 5(d) plots the schematic diagram of a homemade microscopy setup to excite and accurately measure the PSL emission characteristics of each point in the CAO:Eu^{2+},Sm^{3+}/PDMS film before and after the mechanical stimulation. A 980 nm excitation laser is focused onto a surface of the film through a 50× objective lens. Light-emitting from the film surface is collected through the same objective lens, and the collected light is then coupled to either a spectrum analyzer or a CCD camera. Figure 5(e) shows PSL images of one point of the CAO:Eu^{2+},Sm^{3+}/PDMS film before the mechanical stimulation and PSL images of representative position ⑥ marked in Fig. 5(c) of CAO:Eu^{2+},Sm^{3+}/PDMS film after the mechanical stimulation. Also, the corresponding PSL spectra are shown in Fig. 5(f). Furthermore, the PSL images of positions ①, ②, ③, ④, and ⑤ marked in Fig. 5(c) of CAO:Eu^{2+},Sm^{3+}/PDMS film after the mechanical stimulation are displayed in Fig. S9 in the ESM.

As depicted in Fig. S10 in the ESM, the positions of PSL peaks corresponding to different positions are consistent, but the PSL intensities corresponding to the light and dark fringes in Fig. 5(c) are different. Since the number of carriers stored in the trap centers is constant, a different method of subtracting the PSL intensity of the CAO:Eu^{2+},Sm^{3+}/PDMS film after the mechanical stimulation from the PSL intensity before the mechanical stimulation (ΔI = Before − After) is proposed to quantitatively calculate the stress distribution information inside the engine bearing. Figure 5(g) provides the PSL intensity and the corresponding difference of the CAO:Eu^{2+},Sm^{3+}/PDMS film at different positions marked in Fig. 5(c) before and after the mechanical stimuli. Therefore, the stress information recording of the closed mechanical structures by the ML materials with the defect engineering regulation is successfully realized. In addition, the recording and readout of a stress signal can be repeated after 980 nm irradiation as long as the film is not damaged (Fig. 5(h)), and work effectively in a variety of environments, such as aqueous solutions and machinery oil (Fig. S11 in the ESM).

4 Conclusions

In conclusion, a delayed stress memory strategy was proposed to record the stress distribution information of the closed mechanical structure by recording the PSL intensity difference of the flexible CAO:Eu^{2+},Sm^{3+}/PDMS film at the positions with and without the mechanical stimulation after a period of time. It was successfully applied to bearings and gears in the engine, which presents the accurate stress distribution information with long time storage. Moreover, the concentration and distribution of traps were adjusted by introducing different Ln^{3+} ions (i.e., Dy^{3+}, Tm^{3+}, Nd^{3+}, Y^{3+}, and Sm^{3+}). The results show that the adjustment of trap depth greatly realizes the stable preserved energy of the captured carriers and improves accuracy of ML information.

Acknowledgements

This work was financially supported by the National Natural Science Foundation of China (No. 61965012), Project of Yunnan Provincial Natural Science Foundation (Nos. 202001AS070008, 202101AT070126), Yunnan Ten Thousand Talents Plan Young & Elite Talents Project (No. YNWR-QNBJ-2018-295), the Excellent Youth Project of Yunnan Province Applied Basic Research Project (No. 2019FI001), Rare and Precious Metal Materials Genome Engineering Project of Yunnan Province (No. 202002AB080001), and Sichuan Natural Science Foundation (No. 2022JDJQ0030).

Declaration of competing interest

The authors have no competing interests to declare that are relevant to the content of this article.

Electronic Supplementary Material

Supplementary material is available in the online version of this article at https://doi.org/10.1007/s40145-022-0614-2.

References

[1] Petit RR, Michels SE, Feng A, *et al*. Adding memory to pressure-sensitive phosphors. *Light Sci Appl* 2019, **8**: 124.

[2] Wang XD, Peng DF, Huang BL, *et al*. Piezophotonic effect based on mechanoluminescent materials for advanced flexible optoelectronic applications. *Nano Energy* 2019, **55**: 389–400.

[3] Zhang JC, Wang XS, Marriott G, *et al*. Trap-controlled mechanoluminescent materials. *Prog Mater Sci* 2019, **103**: 678–742.

[4] Chen CJ, Zhuang YX, Tu D, *et al*. Creating visible-to-near-infrared mechanoluminescence in mixed-anion compounds $SrZn_2S_2O$ and SrZnSO. *Nano Energy* 2020, **68**: 104329.

[5] Wei XY, Wang XD, Kuang SY, *et al*. Dynamic triboelectrification-induced electroluminescence and its use in visualized sensing. *Adv Mater* 2016, **28**: 6656–6664.

[6] Wang XD, Zhang HL, Yu RM, *et al*. Dynamic pressure mapping of personalized handwriting by a flexible sensor matrix based on the mechanoluminescence process. *Adv Mater* 2015, **27**: 2324–2331.

[7] Qian X, Cai ZR, Su M, *et al*. Printable skin-driven mechanoluminescence devices via nanodoped matrix modification. *Adv Mater* 2018, **30**: 1800291.

[8] Liu LS, Xu CN, Yoshida A, *et al*. Scalable elasticoluminescent strain sensor for precise dynamic stress imaging and onsite infrastructure diagnosis. *Adv Mater Technol* 2019, **4**: 1800336.

[9] Zhang JC, Pan C, Zhu YF, *et al*. Achieving thermo–mechano–opto-responsive bitemporal colorful luminescence via multiplexing of dual lanthanides in piezoelectric particles and its multidimensional anticounterfeiting. *Adv Mater* 2018, **30**: 1804644.

[10] Wu C, Zeng SS, Wang ZF, *et al*. Efficient mechanoluminescent elastomers for dual-responsive anticounterfeiting device and stretching/strain sensor with multimode sensibility. *Adv Funct Mater* 2018, **28**: 1803168.

[11] Tu D, Xu CN, Kamimura S, *et al*. Ferroelectric $Sr_3Sn_2O_7$:Nd^{3+}: A new multipiezo material with ultrasensitive and sustainable near-infrared piezoluminescence. *Adv Mater* 2020, **32**: 1908083.

[12] Chen B, Zhang X, Wang F. Expanding the toolbox of inorganic mechanoluminescence materials. *Acc Mater Res* 2021, **2**: 364–373.

[13] Xu CN, Watanabe T, Akiyama M, *et al*. Artificial skin to sense mechanical stress by visible light emission. *Appl Phys Lett* 1999, **74**: 1236–1238.

[14] Xu CN, Zheng XG, Akiyama M, *et al*. Dynamic visualization of stress distribution by mechanoluminescence image. *Appl Phys Lett* 2000, **76**: 179–181.

[15] Klein C. Application of pressure sensitive paint (PSP) for the determination of the instantaneous pressure field of models in a wind tunnel. *Aerosp Sci Technol* 2000, **4**: 103–109.

[16] Klein C, Engler RH, Henne U, *et al*. Application of pressure-sensitive paint for determination of the pressure field and calculation of the forces and moments of models in a wind tunnel. *Exp Fluids* 2005, **39**: 475–483.

[17] Xu CN, Yamada H, Wang XS, *et al*. Strong elasticoluminescence from monoclinic-structure $SrAl_2O_4$. *Appl Phys Lett* 2004, **84**: 3040–3042.

[18] Imai Y, Momoda R, Xu CN. Elasticoluminescence of europium-doped strontium aluminate spherical particles dispersed in polymeric matrices. *Mater Lett* 2007, **61**: 4124–4127.

[19] Matsuzawa T, Aoki Y, Takeuchi N, *et al*. A new long phosphorescent phosphor with high brightness, $SrAl_2O_4$:Eu^{2+},Dy^{3+}. *J Electrochem Soc* 1996, **143**: 2670–2673.

[20] Akiyama M, Xu CN, Matsui H, *et al*. Recovery phenomenon of mechanoluminescence from $Ca_2Al_2SiO_7$:Ce by irradiation with ultraviolet light. *Appl Phys Lett* 1999, **75**: 2548–2550.

[21] Kodama N, Takahashi T, Yamaga M, *et al*. Long-lasting phosphorescence in Ce^{3+}-doped $Ca_2Al_2SiO_7$ and $CaYAl_3O_7$ crystals. *Appl Phys Lett* 1999, **75**: 1715–1717.

[22] Wu HY, Hu YH, Ju GF, *et al*. Photoluminescence and thermoluminescence of Ce^{3+} and Eu^{2+} in $Ca_2Al_2SiO_7$ matrix. *J Lumin* 2011, **131**: 2441–2445.

[23] Zhang HW, Terasaki N, Yamada H, *et al*. Mechanoluminescence of europium-doped $SrAMgSi_2O_7$ (A = Ca, Sr, Ba). *Jpn J Appl Phys* 2009, **48**: 04C109.

[24] Van den Eeckhout K, Smet PF, Poelman D. Persistent luminescence in Eu^{2+}-doped compounds: A review. *Materials* 2010, **3**: 2536–2566.

[25] Liu B, Shi CS, Yin M, *et al*. The trap states in the $Sr_2MgSi_2O_7$ and (Sr,Ca)$MgSi_2O_7$ long afterglow phosphor activated by Eu^{2+} and Dy^{3+}. *J Alloys Compd* 2005, **387**: 65–69.

[26] Zhang HW, Xu CN, Terasaki N, *et al*. Electro-mechano-optical luminescence from $CaYAl_3O_7$:Ce. *Electrochem Solid-State Lett* 2011, **14**: J76.

[27] Kamimura S, Yamada H, Xu CN. Development of new elasticoluminescent material $SrMg_2(PO_4)_2$:Eu. *J Lumin* 2012, **132**: 526–530.

[28] Ju GF, Hu YH, Chen L, *et al*. Persistent luminescence properties of $SrMg_2(PO_4)_2$:Eu^{2+},Tb^{3+}. *Appl Phys A* 2014, **114**: 867–874.

[29] Tu D, Xu CN, Yoshida A, *et al*. $LiNbO_3$:Pr^{3+}: A multipiezo material with simultaneous piezoelectricity and sensitive piezoluminescence. *Adv Mater* 2017, **29**: 1606914.

[30] Yang XX, Liu R, Xu XH, *et al*. Effective repeatable mechanoluminescence in heterostructured $Li_{1-x}Na_xNbO_3$:Pr^{3+}. *Small* 2021, **17**: 2103441.

[31] Sang JK, Zhou JY, Zhang JC, *et al*. Multilevel static–dynamic anticounterfeiting based on stimuli-responsive luminescence in a niobate structure. *ACS Appl Mater Interfaces* 2019, **11**: 20150–20156.

[32] Zhang JC, Long YZ, Yan X, *et al*. Creating recoverable mechanoluminescence in piezoelectric calcium niobates through Pr^{3+} doping. *Chem Mater* 2016, **28**: 4052–4057.

[33] Pan C, Zhang JC, Zhang M, *et al*. Trap-controlled mechanoluminescence in Pr^{3+}-activated $M_2Nb_2O_7$ (M = Sr, Ca) isomorphic perovskites. *Opt Mater Express* 2018, **8**: 1425.

[34] Wang X, Xu CN, Yamada H, *et al*. Electro-mechano-optical conversions in Pr^{3+}-doped $BaTiO_3$–$CaTiO_3$ ceramics. *Adv Mater* 2005, **17**: 1254–1258.

[35] Zhang JC, Wang XS, Yao X. Enhancement of luminescence and afterglow in $CaTiO_3$:Pr^{3+} by Zr substitution for Ti. *J Alloys Compd* 2010, **498**: 152–156.

[36] Fan XH, Zhang JC, Zhang M, *et al*. Piezoluminescence from ferroelectric $Ca_3Ti_2O_7:Pr^{3+}$ long-persistent phosphor. *Opt Express* 2017, **25**: 14238–14246.

[37] Botterman J, den Eeckhout KV, de Baere I, *et al*. Mechanoluminescence in $BaSi_2O_2N_2$:Eu. *Acta Mater* 2012, **60**: 5494–5500.

[38] Botterman J, van den Eeckhout K, Bos AJJ, *et al*. Persistent luminescence in $MSi_2O_2N_2$:Eu phosphors. *Opt Mater Express* 2012, **2**: 341.

[39] Zhang JC, Xu CN, Long YZ. Elastico-mechanoluminescence in $CaZr(PO_4)_2:Eu^{2+}$ with multiple trap levels. *Opt Express* 2013, **21**: 13699–13709.

[40] Kamimura S, Yamada H, Xu CN. Strong reddish-orange light emission from stress-activated $Sr_{n+1}Sn_nO_{3n+1}:Sm^{3+}$ (n = 1, 2, ∞) with perovskite-related structures. *Appl Phys Lett* 2012, **101**: 091113.

[41] Wang YZ, Huang FT, Luo X, *et al*. The first room-temperature ferroelectric Sn insulator and its polarization switching kinetics. *Adv Mater* 2017, **29**: 1601288.

[42] Tu D, Hamabe R, Xu CN. Sustainable mechanoluminescence by designing a novel pinning trap in crystals. *J Phys Chem C* 2018, **122**: 23307–23311.

[43] Matsui H, Xu CN, Akiyama M, *et al*. Strong mechanoluminescence from UV-irradiated spinels of $ZnGa_2O_4$:Mn and $MgGa_2O_4$:Mn. *Jpn J Appl Phys* 2000, **39**: 6582–6586.

[44] Uheda K, Maruyama T, Takizawa H, *et al*. Synthesis and long-period phosphorescence of $ZnGa_2O_4:Mn^{2+}$ spinel. *J Alloys Compd* 1997, **262–263**: 60–64.

[45] van den Eeckhout K, Poelman D, Smet PF. Persistent luminescence in non-Eu^{2+}-doped compounds: A review. *Mater Basel Switz* 2013, **6**: 2789–2818.

[46] Mukhina MV, Tresback J, Ondry JC, *et al*. Single-particle studies reveal a nanoscale mechanism for elastic, bright, and repeatable ZnS:Mn mechanoluminescence in a low-pressure regime. *ACS Nano* 2021, **15**: 4115–4133.

[47] Zhou H, Du YD, Wu C, *et al*. Understanding the mechanoluminescent mechanisms of manganese doped zinc sulfide based on load effects. *J Lumin* 2018, **203**: 683–688.

[48] Zhang JC, Xu CN, Kamimura S, *et al*. An intense elastico-mechanoluminescence material $CaZnOS:Mn^{2+}$ for sensing and imaging multiple mechanical stresses. *Opt Express* 2013, **21**: 12976–12986.

[49] Zhang JC, Zhao LZ, Long YZ, *et al*. Color manipulation of intense multiluminescence from $CaZnOS:Mn^{2+}$ by Mn^{2+} concentration effect. *Chem Mater* 2015, **27**: 7481–7489.

[50] Huang BL, Peng DF, Pan CF. "Energy Relay Center" for doped mechanoluminescence materials: A case study on Cu-doped and Mn-doped CaZnOS. *Phys Chem Chem Phys* 2017, **19**: 1190–1208.

[51] Tu D, Peng DF, Xu CN, *et al*. Mechanoluminescence properties of red-emitting piezoelectric semiconductor $MZnOS:Mn^{2+}$ (M = Ca, Ba) with layered structure. *J Ceram Soc Jpn* 2016, **124**: 702–705.

[52] Li LJ, Wong KL, Li PF, *et al*. Mechanoluminescence properties of Mn^{2+}-doped BaZnOS phosphor. *J Mater Chem C* 2016, **4**: 8166–8170.

[53] Pan ZW, Lu YY, Liu F. Sunlight-activated long-persistent luminescence in the near-infrared from Cr^{3+}-doped zinc gallogermanates. *Nat Mater* 2012, **11**: 58–63.

[54] Rahimi MR, Yun GJ, Doll GL, *et al*. Effects of persistent luminescence decay on mechanoluminescence phenomena of $SrAl_2O_4:Eu^{2+},Dy^{3+}$ materials. *Opt Lett* 2013, **38**: 4134–4137.

[55] Zhang JC, Fan XH, Yan X, *et al*. Sacrificing trap density to achieve short-delay and high-contrast mechanoluminescence for stress imaging. *Acta Mater* 2018, **152**: 148–154.

[56] Qu BY, Zhang B, Wang L, *et al*. Mechanistic study of the persistent luminescence of $CaAl_2O_4$:Eu,Nd. *Chem Mater* 2015, **27**: 2195–2202.

[57] Hörkner W, Müller-Buschbaum H. Zur kristallstruktur von $CaAl_2O_4$. *J Inorg Nucl Chem* 1976, **38**: 983–984.

[58] Wang L, Wang YH, Xu XH. Effects of Sr^{2+} doping on the persistent luminescence properties of $CaAl_2O_4:Eu^{2+},Nd^{3+}$. *J Appl Phys* 2008, **104**: 013519.

[59] Qiao JW, Ning LX, Molokeev MS, *et al*. Eu^{2+} site preferences in the mixed cation $K_2BaCa(PO_4)_2$ and thermally stable luminescence. *J Am Chem Soc* 2018, **140**: 9730–9736.

[60] Xiang JM, Zheng JM, Zhou ZW, *et al*. Enhancement of red emission and site analysis in Eu^{2+} doped new-type structure $Ba_3CaK(PO_4)_3$ for plant growth white LEDs. *Chem Eng J* 2019, **356**: 236–244.

[61] Piao SQ, Wang YC, Zhou XF, *et al*. Defect engineering in a Eu^{2+}-doped β-Al_2O_3 structure blue phosphor and its controllable zero-thermal quenching luminescence. *ACS Sustainable Chem Eng* 2021, **9**: 7882–7890.

[62] Li X, Wang XS, Hu R, *et al*. Modulating trap levels via co-doping Ca^{2+}/Si^{4+} in $LiTaO_3:Pr^{3+}$ to improve both the intensity and threshold of mechanoluminescence. *J Alloys Compd* 2022, **896**: 162877.

[63] Tian BR, Wang ZF, Smith AT, *et al*. Stress-induced color manipulation of mechanoluminescent elastomer for visualized mechanics sensing. *Nano Energy* 2021, **83**: 105860.

[64] Kim YH, Arunkumar P, Kim BY, *et al*. A zero-thermal-quenching phosphor. *Nat Mater* 2017, **16**: 543–550.